HHS Public Access

Author manuscript

Eur J Nucl Med Mol Imaging. Author manuscript; available in PMC 2015 April 21.

Published in final edited form as:

Eur J Nucl Med Mol Imaging. 2014 November ; 41(11): 2093–2105. doi:10.1007/s00259-014-2830-7.

^{89}Zr-huJ591 immuno-PET imaging in patients with advanced metastatic prostate cancer

Neeta Pandit-Taskar,
Department of Radiology, Memorial Sloan Kettering Cancer Center, New York, NY, USA.
Department of Radiology, Weill Cornell Medical College, New York, NY, USA

Joseph A. O'Donoghue,
Department of Medical Physics, Memorial Sloan Kettering Cancer Center, New York, NY, USA

Volkan Beylergil,
Department of Radiology, Memorial Sloan Kettering Cancer Center, New York, NY, USA

Serge Lyashchenko,
Department of Radiochemistry & Molecular Imaging Probes Core, Memorial Sloan Kettering Cancer Center, New York, NY, USA

Shutian Ruan,
Department of Radiology, Memorial Sloan Kettering Cancer Center, New York, NY, USA

Stephen B. Solomon,
Department of Radiology, Memorial Sloan Kettering Cancer Center, New York, NY, USA.
Department of Radiology, Weill Cornell Medical College, New York, NY, USA

Jeremy C. Durack,
Department of Radiology, Memorial Sloan Kettering Cancer Center, New York, NY, USA.
Department of Radiology, Weill Cornell Medical College, New York, NY, USA

Jorge A. Carrasquillo,
Department of Radiology, Memorial Sloan Kettering Cancer Center, New York, NY, USA.
Department of Radiology, Weill Cornell Medical College, New York, NY, USA

Robert A. Lefkowitz,
Department of Radiology, Memorial Sloan Kettering Cancer Center, New York, NY, USA.
Department of Radiology, Weill Cornell Medical College, New York, NY, USA

Mithat Gonen,
Department of Epidemiology & Biostatistics, Memorial Sloan Kettering Cancer Center, New York, NY, USA

Correspondence to: Neeta Pandit-Taskar, pandit-n@mskcc.org.

Present Address: J. P. Holland, Department of Radiology of Massachusetts General Hospital, Harvard Medical School, Boston, MA, USA

Neeta Pandit-Taskar and Joseph A. O'Donoghue are co-first authors
Michael J. Morris and Steven M. Larson are co-last authors

Conflicts of interest None.

Jason S. Lewis,
Department of Radiology, Memorial Sloan Kettering Cancer Center, New York, NY, USA. Department of Radiochemistry & Molecular Imaging Probes Core, Memorial Sloan Kettering Cancer Center, New York, NY, USA. Program in Molecular Pharmacology and Chemistry, Memorial Sloan Kettering Cancer Center, New York, NY, USA. Department of Radiology, Weill Cornell Medical College, New York, NY, USA

Jason P. Holland,
Department of Radiology, Memorial Sloan Kettering Cancer Center, New York, NY, USA

Sarah M. Cheal,
Department of Radiology, Memorial Sloan Kettering Cancer Center, New York, NY, USA

Victor E. Reuter,
Department of Pathology, Memorial Sloan Kettering Cancer Center, New York, NY, USA. Department of Pathology, Weill Cornell Medical College, New York, NY, USA

Joseph R. Osborne,
Department of Radiology, Weill Cornell Medical College, New York, NY, USA

Massimo F. Loda,
Dana-Farber Cancer Institute, Boston, MA, USA. Broad Institute of Harvard and MIT, Cambridge, MA, USA

Peter M. Smith-Jones,
Department of Psychiatry and Behavioral Science of Stony Brook University, Stony Brook, NY, USA

Wolfgang A. Weber,
Department of Radiology, Memorial Sloan Kettering Cancer Center, New York, NY, USA. Program in Molecular Pharmacology and Chemistry, Memorial Sloan Kettering Cancer Center, New York, NY, USA. Department of Radiology, Weill Cornell Medical College, New York, NY, USA

Neil H. Bander,
Department of Surgery, Memorial Sloan Kettering Cancer Center, New York, NY, USA. Department of Urology, Weill Cornell Medical College, New York, NY, USA

Howard I. Scher,
Department of Medicine, Memorial Sloan Kettering Cancer Center, New York, NY, USA. Department of Medicine, Weill Cornell Medical College, New York, NY, USA

Michael J. Morris, and
Department of Medicine, Memorial Sloan Kettering Cancer Center, New York, NY, USA. Department of Medicine, Weill Cornell Medical College, New York, NY, USA

Steven M. Larson
Department of Radiology, Memorial Sloan Kettering Cancer Center, New York, NY, USA. Program in Molecular Pharmacology and Chemistry, Memorial Sloan Kettering Cancer Center, New York, NY, USA. Department of Radiology, Weill Cornell Medical College, New York, NY, USA

Neeta Pandit-Taskar: pandit-n@mskcc.org

Abstract

Purpose—Given the bone tropism of prostate cancer, conventional imaging modalities poorly identify or quantify metastatic disease. ^{89}Zr-huJ591 positron emission tomography (PET) imaging was performed in patients with metastatic prostate cancer to analyze and validate this as an imaging biomarker for metastatic disease. The purpose of this initial study was to assess safety, biodistribution, normal organ dosimetry, and optimal imaging time post-injection for lesion detection.

Methods—Ten patients with metastatic prostate cancer received 5 mCi of ^{89}Zr-huJ591. Four whole-body scans with multiple whole-body count rate measurements and serum activity concentration measurements were obtained in all patients. Biodistribution, clearance, and lesion uptake by ^{89}Zr-huJ591 immuno-PET imaging was analyzed and dosimetry was estimated using MIRD techniques. Initial assessment of lesion targeting of ^{89}Zr-huJ591 was done. Optimal time for imaging post-injection was determined.

Results—The dose was well tolerated with mild chills and rigors seen in two patients. The clearance of ^{89}Zr-huJ591 from serum was bi-exponential with biological half-lives of 7 ± 4.5 h (range 1.1–14 h) and 62 ± 13 h (range 51–89 h) for initial rapid and later slow phase. Whole-body biological clearance was 219 ± 48 h (range 153–317 h). The mean whole-body and liver residence time was 78.7 and 25.6 h, respectively. Dosimetric estimates to critical organs included liver 7.7 ± 1.5 cGy/mCi, renal cortex 3.5 ± 0.4 cGy/mCi, and bone marrow 1.2 ± 0.2 cGy/mCi. Optimal time for patient imaging after injection was 7 ± 1 days. Lesion targeting of bone or soft tissue was seen in all patients. Biopsies were performed in 8 patients for a total 12 lesions, all of which were histologically confirmed as metastatic prostate cancer. One biopsy-proven lesion was not positive on ^{89}Zr-huJ591, while the remaining 11 lesions were ^{89}Zr-huJ591 positive. Two biopsy-positive nodal lesions were noted only on ^{89}Zr-huJ591 study, while the conventional imaging modality was negative.

Conclusion—^{89}Zr-huJ591 PET imaging of prostate-specific membrane antigen expression is safe and shows good localization of disease in prostate cancer patients. Liver is the critical organ for dosimetry, and 7 ± 1 days is the optimal imaging time. A larger study is underway to determine lesion detection in an expanded cohort of patients with metastatic prostate cancer.

Keywords

^{89}Zr-huJ591; J591 antibody; Prostate cancer; Radioimmunotherapy; Dosimetry

Introduction

The axial skeleton is the most frequent site of prostate cancer metastases, which appear as sclerotic areas on conventional imaging like radiographs and CT scans, and as areas of uptake on standard bone scintigraphy. Current imaging challenges include that imaging has limited sensitivity in detecting early metastatic spread, distinguishing active cancer, and in monitoring posttreatment changes. While a number of imaging agents and radiopharmaceuticals including a variety of novel positron emission tomography (PET)

tracers and small molecules have been used to image prostate cancer, the sensitivity and specificity to detect early metastases, viable disease, and monitor treatment is not optimal [1–4]. A number of small molecules that target gastrin peptide receptors or are directed towards prostate-specific membrane antigen (PSMA) have been investigated [5–9]. However, currently the data is limited for their use in prostate cancer. Given limitations of current modalities, there is a need to develop targeted imaging probes that will allow accurate assessment of viable disease. Development of targeted imaging that is specific for prostate cancer is therefore key.

PSMA is a transmembrane glycoprotein expressed by both benign and malignant prostatic epithelial cells [10] but expressed by virtually all prostate cancers [11] and is expressed in neovasculature of tumors [12]. J591 is a humanized monoclonal antibody (mAb) that targets the extracellular domain of PSMA [13, 14]. Upon binding PSMA, the J591-PSMA complex is rapidly internalized [15]. Previously we have shown imaging and targeting of metastatic prostate cancer and the neovasculature of solid tumors in vivo with ^{111}In-J591 [16–18].

Pilot studies to evaluate safety and biodistribution in patients with prostate cancer showed J591 was safe to administer, localized to bone and soft tissue metastatic sites, and exhibited dose-dependent hepatic uptake [13, 14, 16, 18–21]. These studies were done using gamma-emitting radiolabeled antibody including ^{111}In-J591 and ^{177}Lu-J591. While more specific targeted assessment of disease as compared to conventional imaging was possible, the ability to quantify disease burden is still limited with these and therefore a need for improved imaging methods exists.

PET has better sensitivity and higher resolution as compared to single photon imaging. Additionally, it is a superior quantitative imaging tool, so that tracer uptake in normal organs and tumors is more readily measured, leading to improved estimates of radiation dosimetry. ^{89}Zr is an attractive metalloradionuclide for use in immuno-PET due to favorable decay characteristics, including a physical half-life of 78.4 h appropriate for kinetics of tumor uptake for IgG. Standardized methods for the routine production and isolation of ^{89}Zr using a small cyclotron have been reported [22], and chelation methodology using desferrioxamine-*p*-SCN (DFO) has been described [23, 24]. Preclinical studies with ^{89}Zr-huJ591 have demonstrated excellent targeting in vivo [24].

We undertook this phase I study as an initial step in the validation of ^{89}Zr-huJ591 as a biomarker to determine its biological and performance characteristics. We evaluated safety, biodistribution, and kinetics of ^{89}Zr-huJ591 in patients with metastatic prostate cancer. We also provide radiation dose estimates for normal tissues for ^{89}Zr-huJ591 and a preliminary assessment of lesion targeting. This will be the first reported data on the use of ^{89}Zr-huJ591 in patients with metastatic prostate cancer.

Materials and methods

Patients

A total of ten consecutive patients with metastatic biopsy-proven prostate cancer were studied prospectively. All patients had progression of disease as determined by rising

prostate-specific antigen (PSA), increase in lesions on bone scan, or an increase in measurable soft tissue disease or appearance of new sites of disease on CT or MRI (Table 1). All had received prior therapy. All patients signed written informed consent. The protocol was approved by the Institutional Review Board of Memorial Sloan Kettering Cancer Center (MSKCC), the sole study site (Trial registration ID: NCT01543659).

Antibody formulation and injection—J591 was chelated with DFO using a previously described methodology [23]. The manufactured batch of DFO-huJ591 was documented to be sterile, particulate free, with a pH of 7.0, and endotoxin content of less than 5 EU/ml. The mean number of DFO chelate sites per mAb was 2.7. ^{89}Zr radionuclide production and subsequent radiolabeling of the chelated mAb was performed at the MSKCC Radiochemistry and

Molecular Imaging Probes Core Facility using a previously described method [22]. On average, the radiolabeling efficiency was >70 %, the radiochemical purity was >95 % (as determined by instant thin-layer chromatography), and the immunoreactivity was >90 %, as determined by the Lindmo cell binding assay [25]. The ^{89}Zr-huJ591 was administered under IND #114077.

The mean activity administered was 191.3±9 MBq (5.174±0.25 mCi) and the mean mass of radiolabeled DFO-J591 was 1.68 mg (SD=0.11). In order to deliver a total mass of 25 mg J591 antibody, cold carrier nonconjugate J591 was dispensed in an amount equal to 25 mg minus the amount of radiolabeled DFO-J591. The cold antibody was delivered IV over 5 min followed immediately by a 1-min infusion of the radiolabeled antibody. No premedications were administered. Patients were then monitored for 1 h post-injection for reactions that were graded per CTC 3.0.

All patients had a fluorodeoxyglucose (FDG) PET scan, standard transaxial CT and/or MR imaging, and bone scintigraphy within a month prior to imaging with ^{89}Zr-huJ591.

PET imaging

Each patient underwent whole-body PET scans extending from vertex to mid thighs. In patients where skeletal disease was known to be present in lower limbs per conventional imaging, the scan was extended to include entire lower extremities. Four scans were performed on each patient including within 2–4 h on the day of infusion and at approximately 24 h, once within 48–120 h and 144–168 h post-infusion (Fig. 1, study schema). All scans were performed on the same scanner (GE Discovery DSTE) in 3-D mode with 3 min emission time per bed position on the initial day of injection, extending up to 7 min on the last day. A low-dose CT scan was used for attenuation correction, with one single 80 mA CT scan and 10 mA scans performed on the remainder of the days of imaging. Images were reconstructed using iterative reconstruction and attenuation correction.

Image interpretation and lesion detection

All antibody images were independently reviewed by three experienced nuclear medicine physicians. For each patient, whole-body images obtained after each time point were visually and semiquantitatively analyzed. All visualized areas of uptake were graded on a

scale of 1–5 (1=negative, 2=probably negative, 3=equivocal, 4=probably positive, 5 definitely positive) based on uptake in related to adjacent normal region background activity. All areas of abnormal uptake were recorded; grade 4 and 5 lesions were qualified as positive. Baseline FDG, CT scans, and ^{99m}Tc-methylene diphosphonate (MDP) bone scans were reviewed for lesions by separate radiologists who were blinded to the results of the antibody scans. All lesions detected by each modality were recorded separately. The lesions detected by antibody scans and FDG scan, CT, or bone scan were compared.

Lesion biopsy

Up to two lesions were biopsied in each patient who consented to undergo a biopsy. Lesions were first selected by nuclear medicine physicians following a consensus reading based on image analysis and confirmed in consultation with interventional radiology for feasibility of safely obtaining a biopsy. In order to better define the nature of uptake on scans, lesions were selected on the basis of ^{89}Zr-huJ591 scan positivity and FDG PET scan positivity. If feasible, one bone and one soft tissue lesion was biopsied in each patient. The lesions most preferred for biopsy were those that were suspicious on all imaging modalities. Eight patients were biopsied with a total of 12 lesions. All biopsies were obtained within 2 weeks following ^{89}Zr-huJ591 imaging. The tissue was examined for malignant disease by a pathologist.

Whole-body clearance measurements—Whole-body clearance was determined by serial measurements of count rate using a 12.7 cm (5 in.) thick thallium-activated sodium iodide [NaI (Tl)] scintillation detector at a fixed geometry (3 m from probe to patient). Duplicate anterior and posterior measurements were made and background-corrected geometric mean values were used for clearance curve fitting. Probe measurements were made post-administration before the patients' first void, immediately after the first void, and subsequently at each time when the patient was scanned for a total of five time points. Count rates were normalized to the immediately post-administration value (taken as 100 %) to yield relative retained activities (in %). These data were used to generate clearance curves and calculate kinetic parameters. For quality control purposes, ^{89}Zr standard of known activity was also counted at each measurement time.

Serum clearance measurements—Blood samples were obtained, including a baseline sample prior to ^{89}Zr-huJ591 injection, followed by samples at approximate times of 5, 30, 60, and 120–240 min post-antibody infusion, and subsequently at each time when the patient was scanned for a total of seven time points. Aliquots of serum (typically 500 μl) were measured in duplicate using a NaI(Tl) gamma well-type detector (Wallac Wizard 1480 automatic gamma counter, PerkinElmer) together with appropriate standards. Measured activity concentrations were converted to percent injected dose/liter (% ID/L) and used to generate clearance curves and calculate pharmacokinetic parameters.

Derivation of whole-body and serum kinetic parameters—Effective and biological clearance rates and corresponding half-times were estimated using the SAAM II software application [44]. A mono-exponential function was fitted to the whole-body data and a bi-exponential function was fitted to the serum data. Subsequently, residence times for whole

body (in h) and serum (in h/L), τ, were calculated according to the formula $\tau = \tilde{A}/A_0$ where Ã was the cumulated activity (estimated by integration of the activity-time curve) and A_0 was the administered activity. Additional serum pharmacokinetic parameters that were estimated included Co, volume of distribution of central compartment Vc, AUC to infinity, and clearance.

Determination of uptake in lesions and normal organs—Regions of interest (ROI) were drawn on images for normal organs and selected lesions that were clearly seen in images and were away from the site of blood pool. ROI were combined to generate volumes of interest (VOI) and copied and pasted to all other image sets using software that allowed visualization and cross-linking of multiple image sets (Hermes imaging system, Hermes Medical Solutions, Chicago, IL, USA). A maximum of five lesions per patient were analyzed. In all, a total of 21 bone lesions and 19 soft tissue lesions were analyzed. For purposes of lesion comparison. the maximum values of the lean body mass-adjusted standardized uptake value (SUV_{LBM}-max) were used. These were noted for each lesion at each time point and were used to calculate average values of SUV_{LBM}-max as a function of time for bone lesions, soft tissue lesions, and all lesions combined.

For normal tissues, VOI were used to quantify activity concentration per unit mass (kBq/g) at each time point assuming unit density for all soft tissue organs except lung, the density of which was taken to be 0.3 g/ml. Area under the activity concentration-time curves (AUC) were estimated by trapezoidal integration with areas under the terminal portions calculated by extrapolation from the last measured estimate using the apparent terminal clearance rate or physical decay, whichever was shorter. Subsequently, whole-organ AUC values were estimated using assumed values of organ mass.

Baseline values of organ mass were taken from the OLINDA/EXM software application [45] representing standard man. If the measured patient mass differed by more than 15 % from the standard value (73.7 kg), organ masses were rescaled by multiplying the standard organ mass by the ratio of measured to standard patient masses. Finally, cumulated activities per unit administered activity (i.e., residence times) were derived by dividing the whole-organ AUC values by the administered activity. These were subsequently used as input data for the OLINDA/EXM software application.

In order to examine the ability of PET imaging to quantify vascular ^{89}Zr activity concentration, SUV_{max} in the left atrium was estimated at the first imaging time point and projected to a corresponding serum %ID/L value, based on the measured hematocrit. These were then compared to the gamma well counter-measured %ID/L values for the same post-injection time.

Normal tissue dosimetry—Absorbed radiation doses to various organs including liver, kidney, lung, red marrow, spleen, heart, and whole body were estimated using the OLINDA/EXM software application [45] using estimated residence times as input. Residence times for liver, kidney, lung, and spleen were derived from PET VOI analysis as described above.

The residence time for cardiac contents was calculated by multiplying the serum residence time (in h/L) by the standard or patient mass-rescaled value of cardiac contents volume and by [1-hematocrit (Hct)], where Hct was the measured hematocrit value. The residence time for red marrow was calculated by multiplying the serum residence time by the standard or patient mass-rescaled value of red marrow mass and the factor 0.19, representing the red marrow extracellular fluid fraction, according to the method of Sgouros et al. [46].

The residence time for the remainder of body was derived by subtracting all the individually estimated residence times for normal organs from the whole-body residence time. Normal tissue absorbed dose estimates were calculated for each patient using individualized kinetics. Pharmacokinetic parameters were summarized using descriptive statistics.

Results

Infusion of ^{89}Zr-huJ591

No premedication was given to patients. The injection was tolerated well with only grade 1 infusion-related reactions seen in two of ten patients. Grade 1 chills and rigors occurred in both patients, while one patient also had grade 1 fever. The reactions occurred at 45–50 min post-injection. Patients were treated symptomatically with Benadryl 25–50 mg and Tylenol 650 mg and observed until resolution of all symptoms. There was no significant change in vital signs and no delayed reactions were seen in any patients.

Patient-based analysis

Ten patients with known metastatic prostate cancer were injected with ^{89}Zr-huJ591 (Table 1). ^{89}Zr-huJ591 antibody scans were positive in all patients for either bone and/or soft tissue lesions (Fig. 2). Bony lesions were seen in seven of ten patients by ^{89}Zr-J591 as compared to eight of ten for CT, six of ten for FDG PET scan, and seven of ten for bone scans. ^{89}Zr-huJ591 identified nodal disease in eight of ten patients as compared to six of ten for CT scans and four of ten for FDG PET scans. In one patient, a single site of disease was identified only by ^{89}Zr-huJ591 scan, whereas bone, FDG, and CT scans were negative for both bone and soft tissue (Fig. 3). In an additional patient, ^{89}Zr-huJ591 scan showed nodal disease, while FDG PET and CT scans were negative for soft tissue/nodal disease. In three patients, ^{89}Zr-huJ591 scan showed a significantly larger number of bone lesions as compared to CT, FDG PET, or bone scans (Fig. 2).

Visual analysis and lesion detection

All four imaging time points for ^{89}Zr-huJ591 scans in all patients were graded on a scale of 1–5 for lesion visualization. In nine of ten patients no significant uptake was seen in lesions (was graded 1–2) during the initial 2 days of imaging. Seven of ten patients showed lesions between days 4–6 of imaging; however, the lesions were less conspicuous (grade 3–4) and lesser in number as compared to day 7–8 imaging (Fig. 4). An increased number of lesions and improved uptake (grade 4 or 5) were seen on day 7 or 8 in all patients.

In the 10 patients a total of 180 bone and 35 soft tissue lesions were seen combined on all images on all imaging modalities utilized; ^{89}Zr-huJ591 showed targeting to a total of 199 lesions with 76 in bone and 23 in soft tissue.

Lesion biopsies and pathology correlation (Table 2)

In total 12 lesions were biopsied including 5 bony, 6 nodal and 1 lung lesions. All lesions were confirmed as metastatic disease on pathology. Of 12 lesions, 11 were positive on ^{89}Zr-huJ591 imaging, while only 9 of these lesions were positive on FDG PET scan [26]. One supraclavicular node was negative on both ^{89}Zr-huJ591 imaging and CT imaging (1.1 × 0.8 cm) but was positive on FDG PET scan. In two patients ^{89}Zr-huJ591 imaging revealed biopsy-confirmed soft tissue

Whole-body and serum kinetics—The clearance of activity from the whole body and serum conformed well to mono-and bi-exponential functions, respectively. The average whole-body effective clearance half-time was 57.3±3.2 h (range 52.9–62.8 h) corresponding to a biological clearance half-time of 219±48 h (range 163–317 h) [27].

Serum clearance was characterized by an initial rapid phase (12.7±3.6 %ID/L) followed by a later slow phase (18.6±4.0 %ID/L). Average effective and biological half-times were, respectively, 6.3±3.9 h (range 1–11.6 h) and 7.1±4.6 h (range 1.1–13.7 h) for the fast component and 34.2±3.7 h (range 30.8–41.7 h) and 61.6±13 h (range 50.8–89 h) for the slow component (Fig. 5a, b). The mean AUC was 18±4.8 h/L, C_{max} was 31.3±3.5 %ID/L and Vd was 3.23±0.38 L. The mean whole-body and liver residence time was 78.7 and 25.6 h, respectively

Quantitative image analysis

The lesion uptake was highest at the last imaging performed between days 6 and 8 for all patients (Table 3a). Some nodal lesions showed higher uptake in earlier image sets, probably due to small size and proximity to major vessels. Overall uptake was higher for bone lesions as compared to soft tissue. For bone lesions SUV_{LBM}-max ranged from 3.3 to 29.8 with a mean value of 11.3±1.7 (SEM) and median of 8.2 and that for soft tissue lesions ranged from 1.4 to 10.61 with a mean value of 5.0±0.5 (SEM) and a median of 4.1. The lesion sizes with positive ^{89}Zr-huJ591 imaging varied from 0.8 × 0.7 cm to 2.4 × 2.3 cm for soft tissue lesions.

For normal organs, visual uptake and SUV_{LBM}-max in liver increased with time until the last time point, where it reached an average value of 8.0 (SEM 0.5). Renal uptake increased up to 96 h post-injection, with SUV_{LBM}-max reaching an average of 4.1 (SEM 0.3), and decreased thereafter (Table 3b). Maximal uptake for other organs including spleen, SUV_{LBM}=4.6 (SEM 0.3), and lung, SUV_{LBM}=3.5 (SEM 0.3), was seen immediately post-injection, was primarily determined by activity in the blood pool, and decreased at later imaging. The distribution of tracer showed prominent cardiac blood pool and vascular activity on the day of administration and at the 24-h scan, diminishing thereafter. Gastrointestinal (GI) activity was variable amongst patients with mild activity seen in the earlier scans and maximal activity seen variably in patients between days 4 and 8.

Gallbladder activity was seen in four patients in early scans. Mild physiological adrenal gland activity was seen in two patients.

Low-level uptake was seen in normal bone mean SUV_{max} 1.7 (range 0.4–2.6) and was considered to be nonspecific. In general, the distribution pattern over time showed a progressive increase in uptake in the lesions, greater in bones than soft tissue (Table 3), along with a concomitant decrease in background blood pool and normal organ uptake with the exception of liver. Based on SUV, lesion to background ratio, and visual lesion detection analysis, the best time point for antibody imaging was 7±1 day.

For purposes of quantification of serum activity concentration, the mean PET SUV_{max}-based %ID/L for ten patients (27.0±4.1) was not significantly different from the mean gamma well counter-based %ID/L (29.7±6.6) (paired *t* test, p=0.1833).

Normal tissue dosimetry

Estimates of absorbed doses are provided in Table 4. Notable organ doses in mGy/Mbq include the following: Liver was the organ with maximum dose, estimated at 2.08± 0.42 (7.7±1.5 cGy/mCi), followed by kidney 0.95±0.1 (3.5±0.4 cGy/mCi), heart wall 0.86±0.1 (3.2±0.4 cGy/mCi), spleen 0.74±0.1 (2.7±0.5 cGy/mCi), and bone marrow 0.32±0.05 (1.2±0.2 cGy/mCi). The effective dose was 0.38±0.04 mSv/MBq (1.4±0.2 rem/mCi).

Discussion

Imaging prostate cancer is a clinical challenge particularly in bone which is the most common site of metastatic spread. Current conventional bone imaging is a function of bone turnover which may reflect not only adjacent tumor but also from inflammation, trauma, and/or metabolic disease of bone. As a direct result of the conventional approach to bone imaging, these studies are limited in their ability to detect early tumor spread to bone, assess viable disease, and monitor response to therapy. Other tracers like radiolabeled choline, acetate, and anti-1-amino-3-[^{18}F]fluoro-cyclobutane-1-carboxylic acid (FACBC) have been evaluated, and newer small molecules that target gastrin receptors and PSMA are being evaluated [3–7, 9, 28, 29]. However, none have been assessed as biomarkers and are not yet universally accepted for clinical imaging. Amongst all, ^{11}C-choline has been studied extensively. However, there are a number of practical limitations to its use including a short half-life and the need for onsite cyclotron. The specificity may be limited in some patients [30]. In addition, the role of ^{11}C-choline to detect viable disease and monitor treatment is limited [31, 32]. Background marrow activity may limit detection of bone metastasis.

PET imaging using the radiolabeled amino acid analog ^{18}F-FACBC has been used to detect prostate cancer sites with variable results [4, 33, 34]. In a recent study, it showed higher sensitivity (90 %) for prostatic bed recurrence; however, the specificity was only 40 %. Also, the sensitivity for extraprostatic disease was significantly low at 55 % [4]. The prominent uptake in liver and pancreas and generalized uptake in marrow may limit assessment of lesions [35]. Small molecules and peptides like ^{18}F-DCFBC and those targeting gastrin-releasing peptide receptor (GRPR), namely, bombesin analogs or antagonists, have also recently been explored [5, 36–39]. The imaging has been evaluated in

preclinical or small clinical studies. Imaging experience with these tracers is limited to preclinical or small patient studies. Due to faster clearance from the blood, a better contrast in earlier time point post-injection can be achieved enabling early imaging of lesions as compared to larger molecules or antibodies. However, renal excretion with tracer activity in ureters and bladder may also limit assessment in those with low volume disease and prostate bed recurrence with these agents. Although the initial studies with GRPR agonists and antagonists are favorable, the data are currently limited. Biodistribution of GRPR agonists shows prominent liver, GI tract, pancreas, and renal activity, which may be limiting. GRPR antagonists show lower renal activity and faster clearance; however, the uptake in pancreas is prominent. Small molecules like MIP-1095 and ligands directed towards PSMA have also been developed [40, 41] and imaging explored in small studies. The data though favorable are currently limited. These small molecules clear faster and hence imaging can be performed on the same day, in contrast to whole antibodies. However, renal excretion and bowel visualization may also limit assessment in those with low volume disease with these agents [41–43]. Antibodies, like huJ591, due to the specific targeting to PSMA remain of significant interest in evaluation of prostate cancer. As part of our programmatic efforts to develop better imaging biomarkers for advanced prostate cancer, we performed this first pilot evaluation of in vivo imaging in ten prostate cancer patients using ^{89}Zr-huJ591 to detect PSMA-positive disease. The main objective of radioimmunotargeted imaging was to determine in vivo quantitative kinetics including whole-body uptake and clearance, normal tissue distribution, and dosimetry. In addition, an initial evaluation of tumor targeting and detection in comparison to conventional imaging methods currently used at our center for evaluating metastatic prostate cancer was done. An important goal was to determine whether more extensive studies of ^{89}Zr-huJ591 in a larger cohort of patients were warranted.

The ^{89}Zr-huJ591 injections were well tolerated with minimal toxicity, limited to grade 1 infusion reactions in two patients. The ^{89}Zr-huJ591 was initially distributed in the blood pool, and over the course of 6–8 days distributed into liver, kidney, GI tract, and tumor. As determined by tumor to normal background tissue ratios, optimal time of imaging was 7 ± 1 days. The critical organs were liver and kidney, with radiation absorbed dose of 7 cGy/mCi and 3.4 cGy/mCi, respectively. Although not completely elucidated, the mechanism of accumulation in liver is probably related to a combination of cross-reactivity with PSMA and retention of metabolized radiometal. Accumulation in kidney had cortical appearance and there appeared to be limited urinary excretion during the first 2–3 h since post-void whole-body counts were on average 97.8 % (SD 3.4) of their pre-void values.

We found that the imaging characteristics of the radiometal ^{89}Zr-huJ591 were very similar to that of ^{111}In-huJ591, with the advantage that PET imaging had higher resolution and was more quantitative. For both ^{111}In- and ^{89}Zr-labeled antibodies, prominent liver activity was seen. Renal activity was seen with both studies; however, because of the superiority of PET resolution and hybrid imaging, it was possible to determine that the uptake was localized primarily to the cortex in the ^{89}Zr-huJ591 study. The mean whole-body and serum clearances were similar to ^{111}In-huJ591 at the 25-mg antibody dose. Liver was the organ with highest uptake and dose, followed by kidneys, heart, and spleen. The diffuse increased uptake in the liver limits evaluation of the small liver lesions and hence sensitivity. Though the bowel uptake can be moderately prominent and may obscure small lesions in the

vicinity, in general the PET/CT images allow for proper localization of this uptake to bowel. Also, the metastatic disease pattern of prostate cancer does not involve peritoneum or bowel. The uptake in kidneys is primarily cortical and no significant excretion of ^{89}Zr-huJ591 in urine is seen; therefore, interference from ureter or bladder activity for lesion detection is unlikely.

Prior imaging studies with ^{111}In-J591 showed prominent accumulation in the liver at low antibody mass with progressive saturation with increasing antibody mass [16, 18]; an optimal trade-off between increased J591 circulation and liver uptake was obtained with 25 mg total antibody dose [18]. Based on this, we chose 25 mg of antibody mass dose for this imaging study. Using this antibody mass level, the distribution of ^{89}Zr-huJ591 was favorable and imaging was feasible.

We found that tumor uptake and visualization was high at the proposed optimal imaging times. Analysis of a subset of 40 lesions (21 bone and 19 soft tissue), chosen largely by their perspicuity, showed that bone lesions showed significantly larger average SUV_{max} (8.2 ± 6.5) than soft tissue lesions. Overall in comparison to the sum of conventional imaging modalities (CIM), an additional 70 lesions were seen on ^{89}Zr-huJ591. This preliminary assessment of lesion detection in this initial cohort indicates that a significant fraction of these lesions were true-positives comes from the results of 12 biopsied lesions, in which 11 were ^{89}Zr-huJ591 positive. In two patients, occult lesions that were biopsy confirmed were seen only on the ^{89}Zr-huJ591 imaging.

To understand the discrepant lesion uptake patterns that we have seen, the tissues are being analyzed for markers for PSA and PSMA status wherever possible. The supraclavicular node that was negative on ^{89}Zr-huJ591 was positive for metastatic prostate adenocarcinoma of prostate origin. The tumor showed areas of neuroendocrine differentiation in some parts. Unfortunately, the PSA/PSMA staining data for this particular lesion are not available. It is known that the neuroendocrine lesions can derive from prostate cancers upon loss of androgen receptor signaling and these lesions are often PSA and PSMA low/negative; this may have led to lack of uptake of the ^{89}Zr-huJ591. Some bias may occur due to selection criteria based on positivity on ^{89}Zr-huJ591 and FDG scans. In practice, it is difficult to justify biopsy of sites that are not suspicious. We developed these criteria for choosing sites that were suspicious when all imaging results were considered. The sites chosen were prioritized to those positive on ^{89}Zr-huJ591 imaging as well as on other correlative imaging. The biopsy site was ultimately based on lesion accessibility and ease of biopsy as determined by the interventional radiologist. In this initial analysis, of the 12 sites biopsied, there were at least 4 lesions that were negative on at least 1 or more imaging modalities, of which 3 were noted only on ^{89}Zr-huJ591 imaging and 1 was negative on ^{89}Zr-huJ591 imaging. We may be limited in assessing false-positive ^{89}Zr-huJ591 lesions, for which we have used the follow-up imaging to assess true positivity or negativity. The lesion assessment data based on the initial ten patients is a preliminary analysis as the focus in this cohort of patients and this study is biodistribution and dosimetry. The lesion detection, recognizing these limitations, is currently being studied in a larger population and will subsequently be reported in detail.

The study shows feasibility and safe use of ^{89}Zr-huJ591 antibody scan in prostate cancer patients. The biodistribution and organ dosimetry are favorable, allowing imaging at this level of activity administered. Preliminary analysis shows potential value in detecting disease in metastatic prostate cancer patients. Study in an expanded population is being done for evaluation and detailed analysis of the role in detecting disease in those with negative or inconclusive conventional imaging and those with increasing PSA.

Due to the specificity and ability to target PSMA, the use of antibodies in imaging and targeting prostate cancer remains of immense interest. It may have potential in more sensitively detecting lesions in bone, assessing viable disease, and may potentially be useful for assessment of treatment response particularly with antiandrogen therapy.

Conclusion

PET imaging with ^{89}Zr-huJ591 is feasible, safe, well tolerated, and shows favorable biodistribution and acceptable organ dosimetry in patients with advanced prostate cancer. ^{89}Zr-huJ591 antibody targets both bone and soft tissue lesions. ^{89}Zr-huJ591 may help identify disease sites in some patients with equivocal or negative conventional imaging. Further studies are warranted to determine imaging sensitivity, specificity, and accuracy for lesion detection in a larger cohort of metastatic prostate cancer patients.

Acknowledgments

Starr Cancer Consortium, Prostate cancer program of MSKCC and Center for Targeted Radioimmunotherapy and Diagnosis of the Ludwig Center for Cancer Immunotherapy, David H. Koch Foundation, R21 CA153177-03. RMPIC core is supported in part by NIH P30CA008748, the Landy Research Fund, and Hascoe Charitable Foundation.

References

1. Kiess AP, Cho SY, Pomper MG. Translational molecular imaging of prostate cancer. Curr Radiol Rep. 2013; 1(3):216–26. [PubMed: 24159427]
2. Morris MJ, Autio KA, Basch EM, Danila DC, Larson S, Scher HI. Monitoring the clinical outcomes in advanced prostate cancer: what imaging modalities and other markers are reliable? Semin Oncol. 2013; 40(3):375–92. [PubMed: 23806501]
3. Haseebuddin M, Dehdashti F, Siegel BA, Liu J, Roth EB, Nepple KG, et al. 11C-acetate PET/CT before radical prostatectomy: nodal staging and treatment failure prediction. J Nucl Med. 2013; 54(5):699–706. [PubMed: 23471311]
4. Schuster DM, Nieh PT, Jani AB, Amzat R, Bowman FD, Halkar RK, et al. Anti-3-[(18)F]FACBC positron emission tomography-computerized tomography and (111)In-capromab pendetide single photon emission computerized tomography-computerized tomography for recurrent prostate carcinoma: results of a prospective clinical trial. J Urol. 2014; 191(5):1446–53. [PubMed: 24144687]
5. Schroeder RP, van Weerden WM, Krenning EP, Bangma CH, Bemdsen S, Grievink-de Ligt CH, et al. Gastrin-releasing peptide receptor-based targeting using bombesin analogues is superior to metabolism-based targeting using choline for in vivo imaging of human prostate cancer xenografts. Eur J Nucl Med Mol Imaging. 2011; 38(7):1257–66. [PubMed: 21431398]
6. Nanda PK, Pandey U, Bottenus BN, Rold TL, Sieckman GL, Szczodroski AF, et al. Bombesin analogues for gastrin-releasing peptide receptor imaging. Nucl Med Biol. 2012; 39(4):461–71. [PubMed: 22261143]

7. Eder M, Eisenhut M, Babich J, Haberkorn U. PSMA as a target for radiolabelled small molecules. Eur J Nucl Med Mol Imaging. 2013; 40(6):819–23. [PubMed: 23463331]
8. Carlucci G, Ananias HJ, Yu Z, Hoving HD, Helfrich W, Diercks RA, et al. Preclinical evaluation of a novel (111)In-labeled bombesin homodimer for improved imaging of GRPR-positive prostate cancer. Mol Pharm. 2013; 10(5):1716–24. [PubMed: 23590837]
9. Pan D, Xu YP, Yang RH, Wang L, Chen F, Luo S, et al. A new (68)Ga-labeled BBN peptide with a hydrophilic linker for GRPR-targeted tumor imaging. Amino Acids. 2014; 46:1481–9. [PubMed: 24633452]
10. Murphy GP, Elgamal AA, Su SL, Bostwick DG, Holmes EH. Current evaluation of the tissue localization and diagnostic utility of prostate specific membrane antigen. Cancer. 1998; 83(11): 2259–69. [PubMed: 9840525]
11. Bostwick DG, Pacelli A, Blute M, Roche P, Murphy GP. Prostate specific membrane antigen expression in prostatic intraepithelial neoplasia and adenocarcinoma: a study of 184 cases. Cancer. 1998; 82(11):2256–61. [PubMed: 9610707]
12. Haffner MC, Kronberger IE, Ross JS, Sheehan CE, Zitt M, Mühlmann G, et al. Prostate-specific membrane antigen expression in the neovasculature of gastric and colorectal cancers. Hum Pathol. 2009; 40(12):1754–61. [PubMed: 19716160]
13. Bander NH, Trabulsi EJ, Kostakoglu L, Yao D, Vallabhajosula S, Smith-Jones P, et al. Targeting metastatic prostate cancer with radiolabeled monoclonal antibody J591 to the extracellular domain of prostate specific membrane antigen. J Urol. 2003; 170(5):1717–21. [PubMed: 14532761]
14. Bander NH, Nanus DM, Milowsky MI, Kostakoglu L, Vallabahajosula S, Goldsmith SJ. Targeted systemic therapy of prostate cancer with a monoclonal antibody to prostate-specific membrane antigen. Semin Oncol. 2003; 30(5):667–77. [PubMed: 14571414]
15. Liu H, Rajasekaran AK, Moy P, Xia Y, Kim S, Navarro V, et al. Constitutive and antibody-induced internalization of prostate-specific membrane antigen. Cancer Res. 1998; 58(18):4055–60. [PubMed: 9751609]
16. Pandit-Taskar N, O'Donoghue JA, Morris MJ, Wills EA, Schwartz LH, Gonen M, et al. Antibody mass escalation study in patients with castration-resistant prostate cancer using (111)In-J591: lesion detectability and dosimetric projections for (90)Y radioimmunotherapy. J Nucl Med. 2008; 49(7):1066–74. [PubMed: 18552139]
17. Morris MJ, Pandit-Taskar N, Divgi CR, Bender S, O'Donoghue JA, Nacca A, et al. Phase I evaluation of J591 as a vascular targeting agent in progressive solid tumors. Clin Cancer Res. 2007; 13(9):2707–13. [PubMed: 17473203]
18. Morris MJ, Divgi CR, Pandit-Taskar N, Batraki M, Warren N, Nacca A, et al. Pilot trial of unlabeled and indium-111-labeled anti-prostate-specific membrane antigen antibody J591 for castrate metastatic prostate cancer. Clin Cancer Res. 2005; 11(20):7454–61. [PubMed: 16243819]
19. Milowsky MI, Nanus DM, Kostakoglu L, Vallabhajosula S, Goldsmith SJ, Bander NH. Phase I trial of yttrium-90-labeled anti-prostate-specific membrane antigen monoclonal antibody J591 for androgen-independent prostate cancer. J Clin Oncol. 2004; 22(13):2522–31. [PubMed: 15173215]
20. Trabulsi EJ, Yao D, Joyce MA, et al. Phase I radioimmunotherapy (RIT) trials of monoclonal antibody (mAb) J591 to the extracellular domain of prostate specific membrane antigen (PSMA(ext)) radiolabeled with (90)yttrium (Y-90) or (177)lutetium (Lu-177) in advanced prostate cancer (Pca). J Urol. 2003; 169(4):396–7.
21. Nanus DM, Milowsky MI, Kostakoglu L, Smith-Jones PM, Vallabahajosula S, Goldsmith SJ, et al. Clinical use of monoclonal antibody HuJ591 therapy: targeting prostate specific membrane antigen. J Urol. 2003; 170(6):S84–8. [PubMed: 14610416]
22. Holland JP, Sheh Y, Lewis JS. Standardized methods for the production of high specific-activity zirconium-89. Nucl Med Biol. 2009; 36(7):729–39. [PubMed: 19720285]
23. Vosjan MJ, Perk LR, Visser GW, Budde M, Jurek P, Kiefer GE, et al. Conjugation and radiolabeling of monoclonal antibodies with zirconium-89 for PET imaging using the bifunctional chelate p-isothiocyanatobenzyl-desferrioxamine. Nat Protoc. 2010; 5(4):739–43. [PubMed: 20360768]

24. Holland JP, Divilov V, Bander NH, Smith-Jones PM, Larson SM, Lewis JS. 89Zr-DFO-J591 for immunoPET of prostate-specific membrane antigen expression in vivo. J Nucl Med. 2010; 51(8): 1293–300. [PubMed: 20660376]
25. Lindmo T, Boven E, Cuttitta F, Fedorko J, Bunn PA Jr. Determination of the immunoreactive fraction of radiolabeled monoclonal antibodies by linear extrapolation to binding at infinite antigen excess. J Immunol Methods. 1984; 72(1):77–89. [PubMed: 6086763]
26. Morris MJ, Pandit-Taskar N, Carrasquillo JA, O'Donoghue JA, Humm J, Serge K, et al. Phase I trial of zirconium 89 (Zr89) radiolabeled J591 in metastatic castration-resistant prostate cancer (mCRPC). J Clin Oncol. 2013; 31(Suppl 6):abstract 31.
27. Pandit-Taskar N, O'Donoghue J, et al. 89Zr J591 immunoPET imaging in patients with prostate cancer. J Nucl Med. 2013; 54(Suppl 2):287.
28. Lutje S, Boerman OC, van Rij CM, Sedelaar M, Helfrich W, Oyen WJ, et al. Prospects in radionuclide imaging of prostate cancer. Prostate. 2012; 72(11):1262–72. [PubMed: 22127918]
29. Yu Z, Carlucci G, Ananias HJ, Dierckx RA, Liu S, Helfrich W, et al. Evaluation of a technetium-99m labeled bombesin homodimer for GRPR imaging in prostate cancer. Amino Acids. 2013; 44(2):543–53. [PubMed: 22833158]
30. Castellucci P, Picchio M. 11C-choline PET/CTand PSA kinetics. Eur J Nucl Med Mol Imaging. 2013; 40 (Suppl 1):S36–40. [PubMed: 23579864]
31. Ceci F, Castellucci P, Mamede M, Schiavina R, Rubello D, Fuccio C, et al. (11)C-Choline PET/CT in patients with hormone-resistant prostate cancer showing biochemical relapse after radical prostatectomy. Eur J Nucl Med Mol Imaging. 2013; 40(2):149–55. [PubMed: 23151910]
32. Ceci F, Schiavina R, Castellucci P, Brunocilla E, Fuccio C, Colletti PM, et al. 11C-choline PET/CT scan in patients with prostate cancer treated with intermittent ADT: a sequential PET/CT study. Clin Nucl Med. 2013; 38(7):e279–82. [PubMed: 23698461]
33. Nanni C, Schiavina R, Brunocilla E, Borghesi M, Ambrosini V, Zanoni L, et al. 18F-FACBC compared with 11C-choline PET/CT in patients with biochemical relapse after radical prostatectomy: a prospective study in 28 patients. Clin Genitourin Cancer. 2014; 12(2):106–10. [PubMed: 24135632]
34. Turkbey B, Mena E, Shih J, Pinto PA, Merino MJ, Lindenberg ML, et al. Localized prostate cancer detection with 18F FACBC PET/CT: comparison with MR imaging and histopathologic analysis. Radiology. 2014; 270(3):849–56. [PubMed: 24475804]
35. Nye JA, Schuster DM, Yu W, Camp VM, Goodman MM, Votaw JR. Biodistribution and radiation dosimetry of the synthetic nonmetabolized amino acid analogue anti-18F-FACBC in humans. J Nucl Med. 2007; 48(6):1017–20. [PubMed: 17504867]
36. Cho SY, Gage KL, Mease RC, Senthamizhchelvan S, Holt DP, Jeffrey-Kwanisai A, et al. Biodistribution, tumor detection, and radiation dosimetry of 18F-DCFBC, a low-molecular-weight inhibitor of prostate-specific membrane antigen, in patients with metastatic prostate cancer. J Nucl Med. 2012; 53(12):1883–91. [PubMed: 23203246]
37. Wieser G, Mansi R, Grosu AL, Schultze-Seemann W, Dumont-Walter RA, Meyer PT, et al. Positron emission tomography (PET) imaging of prostate cancer with a gastrin releasing peptide receptor antagonist–from mice to men. Theranostics. 2014; 4(4):412–9. [PubMed: 24578724]
38. Dijkgraaf I, Franssen GM, McBride WJ, D'Souza CA, Laverman P, Smith CJ, et al. PET of tumors expressing gastrin-releasing peptide receptor with an 18F-labeled bombesin analog. J Nucl Med. 2012; 53(6):947–52. [PubMed: 22570329]
39. Abiraj K, Mansi R, Tamma ML, Fani M, Forrer F, Nicolas G, et al. Bombesin antagonist-based radioligands for translational nuclear imaging of gastrin-releasing peptide receptor-positive tumors. J Nucl Med. 2011; 52(12):1970–8. [PubMed: 22080443]
40. Afshar-Oromieh A, Zechmann CM, Malcher A, Eder M, Eisenhut M, Linhart HG, et al. Comparison of PET imaging with a (68)Ga-labelled PSMA ligand and (18)F-choline-based PET/CT for the diagnosis of recurrent prostate cancer. Eur J Nucl Med Mol Imaging. 2014; 41(1): 11–20. [PubMed: 24072344]
41. Zechmann CM, Afshar-Oromieh A, Armor T, Stubbs JB, Mier W, Hadaschik B, et al. Radiation dosimetry and first therapy results with a (124)I/(131)I-labeled small molecule (MIP-1095)

targeting PSMA for prostate cancer therapy. Eur J Nucl Med Mol Imaging. 2014; 41:1280–92. [PubMed: 24577951]

42. Hillier SM, Kern AM, Maresca KP, Marquis JC, Eckelman WC, Joyal JL, et al. 123I-MIP-1072, a small-molecule inhibitor of prostate-specific membrane antigen, is effective at monitoring tumor response to taxane therapy. J Nucl Med. 2011; 52(7):1087–93. [PubMed: 21680691]
43. Barrett JA, Coleman RE, Goldsmith SJ, Vallabhajosula S, Petry NA, Cho S, et al. First-in-man evaluation of 2 high-affinity PSMA-avid small molecules for imaging prostate cancer. J Nucl Med. 2013; 54(3):380–7. [PubMed: 23303962]
44. Barrett PH, Bell BM, Cobelli C, Golde H, Schumitzky A, Vicini P, et al. SAAM II: simulation, analysis, and modeling software for tracer and pharmacokinetic studies. Metabolism. 1998; 47(4): 484–92. [PubMed: 9550550]
45. Stabin MG, Sparks RB, Crowe E. OLINDA/EXM: the second-generation personal computer software for internal dose assessment in nuclear medicine. J Nucl Med. 2005; 46(6):1023–7. [PubMed: 15937315]
46. Sgouros G, Stabin M, Erdi Y, Akabani G, Kwok C, Brill AB, et al. Red marrow dosimetry for radiolabeled antibodies that bind to marrow, bone, or blood components. Med Phys. 2000; 27(9): 2150–64. [PubMed: 11011745]

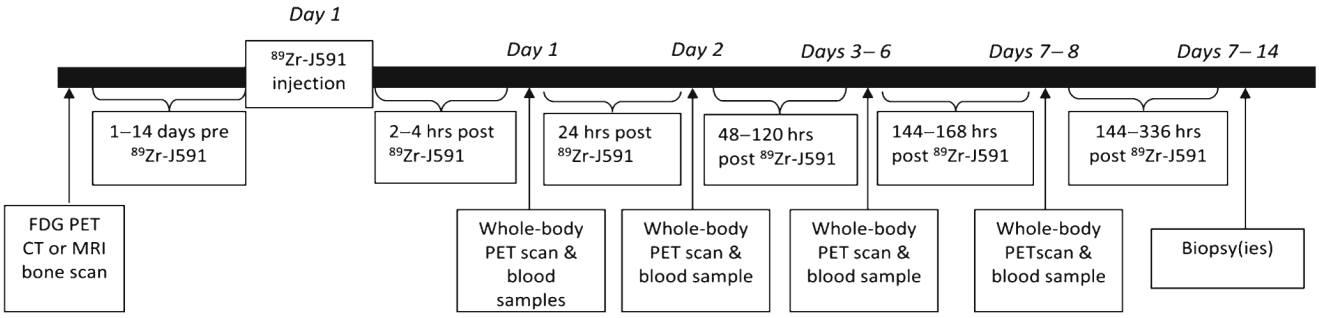

Fig. 1.
^{89}Zr-huJ591 imaging

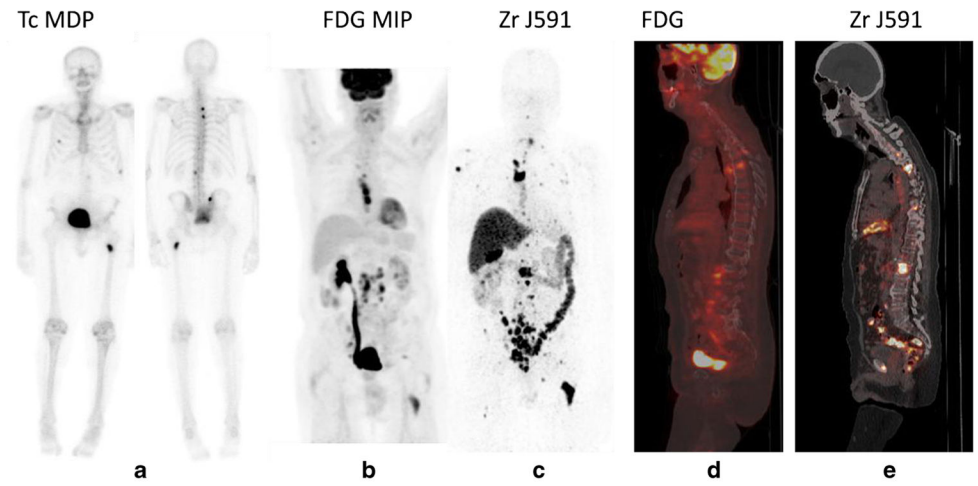

Fig. 2.

Patient with rising PSA was scanned with ^{89}Zr-huJ591 imaging. Anterior and posterior ^{99m}Tc-MDP bone scan (**a**) shows only a few lesions, FDG shows nodal disease in the thorax, retroperitoneum, and pelvic regions and a few bone lesions in spine (**b** and **d**). Overall more bone lesions were seen on ^{89}Zr-huJ591 study than on MIP image and sagittal fused image including multiple vertebrae, pelvic bones, ribs, and humerus. Targeting was also seen to the retroperitoneal and pelvic nodes by ^{89}Zr-huJ591 (**c**, **e**)

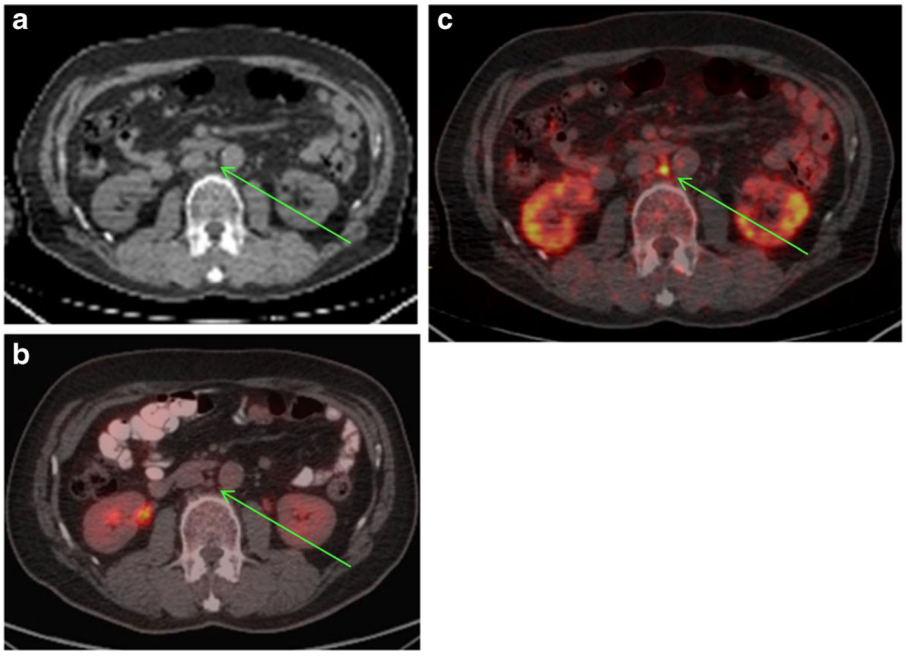

Fig. 3.

^{89}Zr-huJ591 scan shows uptake in subcentimeter retroperitoneal node. Patient with PSA of 4.7 was imaged with ^{89}Zr-huJ591. Transaxial CT images (**a**) show small 4-mm node in the aortocaval region, not considered metastatic. This was not avid on FDG scan (**b**). However, ^{89}Zr-huJ591 image (**c**) shows uptake in the aortocaval node (SUV 6.78). The biopsy of this node was positive for prostatic adenocarcinoma

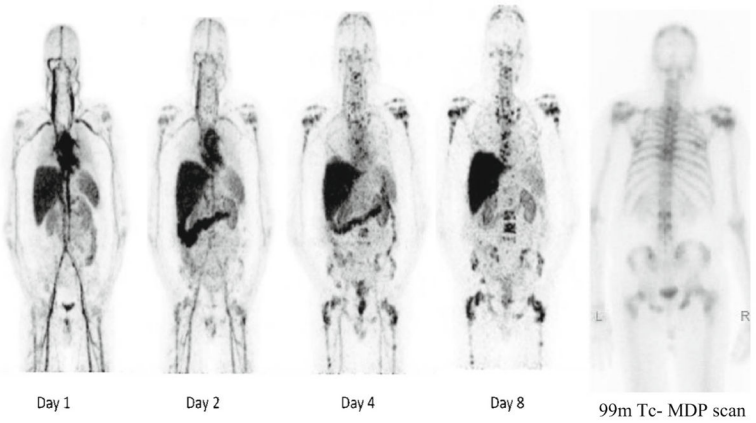

Fig. 4.

Serial whole-body ^{89}Zr-huJ591 scans (MIP images). Images show physiological distribution in cardiac and vascular blood pool, decreasing with time, in liver, spleen, kidneys, and GI tract. Images show increased accumulation in multiple bone lesions, best seen in day 8 image. Many of these lesions are not clearly visualized on ^{99m}Tc-MDP scan (*right*) lesions otherwise not detected by CT or FDG scan; in one patient ^{89}Zr-huJ591 imaged disease was seen on MRI.

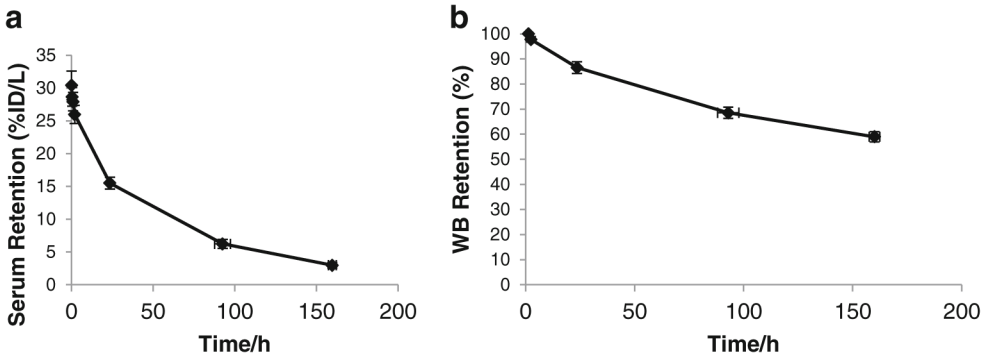

Fig. 5.

Serum and whole-body retention of ^{89}Zr-J591. Average serum retention (**a**) obtained from serum samples counted in a gamma counter. Average whole-body retention (**b**) determined using a NaI probe at fixed geometry from the patient, taking the initial post-void counts as 100 %. The average WB biological clearance half-time was 219±48 h (range 163–317 h)

Table 1

Patient demographics

Characteristic (*n*=10)	**No. (%)**	**Median (range)**
Age		65 (56–79)
Gleason score		8 (7–9)
KPS (%)		90 (80–100)
Disease stage		
Castration-resistant metastatic	7 (70 %)	
Non-castrate metastatic	3 (30 %)	
No. of prior hormonal therapies		1 (0–2)
Prior chemotherapy for mCRPC	2 (20 %)	
Extent of disease by CT, MRI, and bone scan		
Bone only	3 (30 %)	
Bone and lymph node	4 (40 %)	
Lymph node and lung	1 (10 %)	
Lymph node only	2 (20 %)	
PSA (ng/ml)		6.90 (1.09–78.61)

KPS Karnofsky performance status, *mCRPC* metastatic castration-resistant prostate cancer

Table 2

Imaging and pathology correlation for 12 biopsied lesions

Bone biopsy site	^{89}Zr-huJ591 PET	FDG PET	Bone scan	Pathology
L4 vertebra	+	+	+	+
Iliac bone	+	+	+	+
Iliac bone	+	+	+	+
Iliac bone	+	+	+	+
Sacrum	+	+	+	+
Soft tissue biopsy site	^{89}Zr-huJ591 PET	FDG PET	CT scan	Pathology
Mediastinal lymph node	+	+	+	+
Retrocaval lymph node	+	+	+	+
Para-aortic lymph node	+	+	+	+
Aortocaval lymph node	+	−	−	+
Retroperitoneal lymph node	+	−	−	+
Lung nodule	+	−	+	+
Supraclavicular lymph node	−	+	−	+

Table 3

a SUV_{LBM}-max change for organs and lesions. b SUV_{LBM}-max for lesions

A

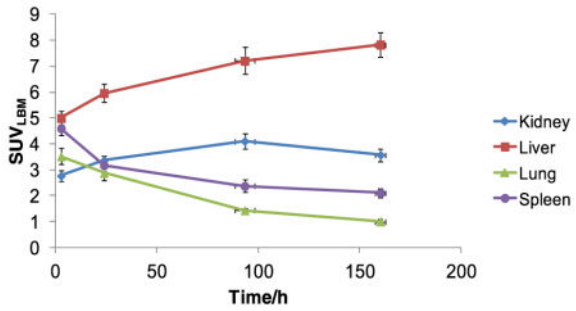

Uptake	(SUV LBM-max) Mean +/−SD	(SUV LBM-max) D6-8
Liver	8 +/− 1.5	8 +/− 1.5
Kidney	4.1 +/− 0.8	3.57 +/− 0.75
Lung	3.52 +/− 1.0	1.01 +/− 0.3
Spleen	4.6 +/− 0.87	2.1 +/− 0.57

B

SUVLBM-max for lesions

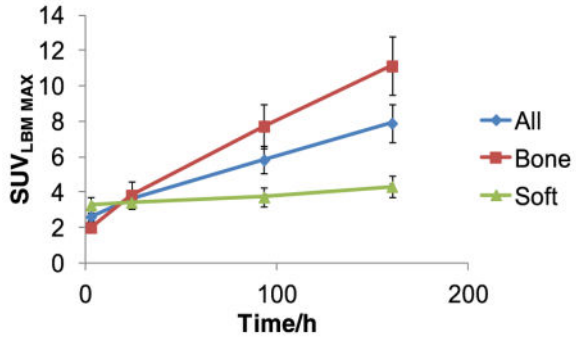

	Bone lesions N=21		Soft tissue lesions N=19	
Time (hr)	Mean	SD	Mean	SD
2.7	1.99	1.3	3.27	1.85
23.9	3.81	3.61	3.41	1.6
93.3	7.73	5.82	3.71	2.31
160.3	11.13	7.57	4.31	2.59

Table 4

Whole-body and organ absorbed doses for ^{89}Zr-huJ591 obtained using residence times calculated from serial PET scans and using OLINDA software

Target organ	Mean (mSv/MBq)	SD (mSv/MBq)	Mean (cGy/mCi)	SD (cGy/mCi)
Adrenals	0.55	0.05	2.03	0.19
Brain	0.14	0.04	0.52	0.16
Breasts	0.22	0.04	0.82	0.13
Gallbladder wall	0.75	0.09	2.76	0.35
LLI wall	0.22	0.06	0.81	0.22
Small intestine	0.29	0.05	1.09	0.20
Stomach wall	0.33	0.05	1.22	0.18
ULI wall	0.33	0.05	1.23	0.18
Heart wall	0.86	0.11	3.17	0.39
Kidneys	0.95	0.12	3.53	0.44
Liver	2.08	0.42	7.69	1.55
Lungs	0.58	0.08	2.14	0.29
Muscle	0.23	0.04	0.85	0.16
Ovaries	0.24	0.06	0.90	0.22
Pancreas	0.50	0.05	1.86	0.19
Red marrow	0.32	0.05	1.19	0.20
Osteogenic cells	0.31	0.07	1.16	0.28
Skin	0.16	0.03	0.57	0.12
Spleen	0.74	0.14	2.72	0.51
Testes	0.16	0.05	0.58	0.18
Thymus	0.31	0.06	1.16	0.21
Thyroid	0.19	0.05	0.69	0.19
Urinary bladder wall	0.21	0.06	0.77	0.21
Uterus	0.24	0.06	0.87	0.22
Total body	0.29	0.04	1.06	0.15
Effective dose equivalent (mSv/MBq)	0.54	0.05		
Effective dose (mSv/MBq)	0.38	0.04		

LLI lower large intestine, *ULI* upper large intestine